American Mineralogist, Volume 101, pages 2723–2730, 2016

High-pressure compressibility and vibrational properties of $(Ca,Mn)CO_3$

JIN LIU[1,*], RAZVAN CARACAS[2], DAWEI FAN[3], EMA BOBOCIOIU[2], DONGZHOU ZHANG[4], AND WENDY L. MAO[1,5]

[1]Department of Geological Sciences, Stanford University, Stanford, California 94305, U.S.A.
[2]CNRS, Laboratoire de Géologie de Lyon, Université Claude Bernard Lyon 1, 69342 Lyon Cedex 07, France
[3]Key Laboratory of High-temperature and High-pressure Study of the Earth's Interior, Institute of Geochemistry, Chinese Academy of Sciences, Guiyang, Guizhou 550002, China
[4]Hawai'i Institute of Geophysics and Planetology, University of Hawai'i at Manoa, Honolulu, Hawaii 96822, U.S.A.
[5]Stanford Institute for Materials and Energy Sciences, SLAC National Accelerator Laboratory, Menlo Park, California 94025, U.S.A.

ABSTRACT

Knowledge of potential carbon carriers such as carbonates is critical for our understanding of the deep-carbon cycle and related geological processes within the planet. Here we investigated the high-pressure behavior of $(Ca,Mn)CO_3$ up to 75 GPa by synchrotron single-crystal X-ray diffraction, laser Raman spectroscopy, and theoretical calculations. $MnCO_3$-rich carbonate underwent a structural phase transition from the $CaCO_3$-I structure into the $CaCO_3$-VI structure at 45–48 GPa, while $CaCO_3$-rich carbonate transformed into $CaCO_3$-III and $CaCO_3$-VI at approximately 2 and 15 GPa, respectively. The equation of state and vibrational properties of $MnCO_3$-rich and $CaCO_3$-rich carbonates changed dramatically across the phase transition. The $CaCO_3$-VI-structured $CaCO_3$-rich and $MnCO_3$-rich carbonates were stable at room temperature up to at least 53 and 75 GPa, respectively. The addition of smaller cations (e.g., Mn^{2+}, Mg^{2+}, and Fe^{2+}) can enlarge the stability field of the $CaCO_3$-I phase as well as increase the pressure of the structural transition into the $CaCO_3$-VI phase.

Keywords: Carbonate, X-ray diffraction, raman spectroscopy, high pressure

INTRODUCTION

Carbonates are the major, oxidized carbon-bearing phases in the Earth's crust and represent an important carrier of carbon back into the mantle. The high-pressure behavior of carbonates is thus essential for understanding deep-carbon cycling and storage in the Earth's deep interior (Dasgupta and Hirschmann 2010; Hazen and Schiffries 2013). All naturally occurring carbonates in the crust can be potentially transported into the deep mantle at subduction zones. In particular, $CaCO_3$ is the dominant carbonate phase in the Earth's crust and has been extensively investigated in static and dynamic high-pressure studies (e.g., Liu and Mernagh 1990; Williams et al. 1992; Biellmann et al. 1993; Gillet et al. 1993; Fiquet et al. 1994; Suito et al. 2001; Ono et al. 2005, 2007; Oganov et al. 2006; Merlini et al. 2012b; Shi et al. 2012; Ishizawa et al. 2013). $CaCO_3$ adopts a rhombohedral $R\bar{3}c$ structure at ambient conditions (referred to as $CaCO_3$-I) and undergoes a series of structural phase transitions upon compression at room temperature into $CaCO_3$-II, $CaCO_3$-III, and $CaCO_3$-VI approximately at 1.7, 2–3, and 15 GPa, respectively (Suito et al. 2001; Catalli and Williams 2005; Merlini et al. 2012b). $CaCO_3$-I, $CaCO_3$-II, and $CaCO_3$-III transform into aragonite at elevated temperatures and then become disordered calcite when approaching the liquidus (Suito et al. 2001), while the phase stability of $CaCO_3$-VI is not well constrained at high pressure and temperature (*P-T*).

At ambient conditions, there is a continuous solid solution between $CaCO_3$ and $MnCO_3$. $MnCO_3$ occurs in the $CaCO_3$-I structure at ambient conditions and its high-pressure behavior has been the subject of debate. The dissociation of $MnCO_3$ was observed at 6–8 GPa and 2273 K (Liu et al. 2001), while other studies found $MnCO_3$ to be stable up to ~47 GPa and 2000 K (Santillan and Williams 2004) and then to transform into an orthorhombic phase at 50 GPa above 1500 K (Ono 2007). Furthermore, a series of transitions in $MnCO_3$ at room temperature were observed at 15 and 50 GPa, respectively (Farfan et al. 2013). In the most recent studies, $MnCO_3$ was observed to transform into the $CaCO_3$-VI structure at room temperature upon compression, although those studies reported a different phase transition pressure of either ~35 GPa (Boulard et al. 2015) or 44 GPa (Merlini et al. 2015). Hereafter the low-pressure ($CaCO_3$-I) and high-pressure ($CaCO_3$-VI) phases of $MnCO_3$ will be referred to as $MnCO_3$-I and $MnCO_3$-II, respectively, after Merlini et al. (2015). Furthermore, the compressibility and vibrational properties of $MnCO_3$-II have not been determined. Here we combine synchrotron single-crystal X-ray diffraction (XRD) and laser Raman spectroscopy, together with theoretical calculations to study the high-pressure behavior of $(Ca,Mn)CO_3$ up to 75 GPa.

METHODS

Natural calcite and rhodochrosite starting samples were obtained from Dabie Mountain, China. Based on electron microprobe analyses, the composition of calcite was determined to be $(Ca_{0.992}Mn_{0.008})CO_3$ with very minor amounts less than 0.1% of Mg and Fe, while the rhodochrosite sample was $(Ca_{0.009}Mn_{0.980}Fe_{0.009}Mg_{0.002})CO_3$. For simplicity, we will herein refer to these two samples as $CaCO_3$ and $MnCO_3$, respectively. Both $CaCO_3$ and $MnCO_3$ starting samples exhibit a rhombohedral shape, reflecting their $R\bar{3}c$ structure.

* E-mail: jinliu1@stanford.edu

Single-crystal X-ray diffraction

Single-crystal XRD analyses confirmed the $CaCO_3$-I structure of the $MnCO_3$ starting sample with lattice parameters a = 4.7762(15) Å and c = 15.6477(68) Å at ambient conditions. A small platelet of single-crystal $MnCO_3$ of ~5 µm thick and ~40 µm in diameter was loaded into a symmetric diamond-anvil cell (DAC). A tungsten (W) gasket was pre-indented by a pair of diamond anvils having 300 µm flat culets to a thickness of ~30 µm. A hole of 170 µm in diameter was drilled in the pre-indented gasket and used as a sample chamber. A small piece of Pt foil was for use as a pressure calibrant. The pressure-transmitting medium, Ne, was loaded into the sample chamber at GSECARS of the Advanced Photon Source (APS), Argonne National Laboratory (ANL). High-pressure single-crystal XRD experiments were conducted at beamline 13-IDD of the APS, ANL, using a monochromatic X-ray beam with a wavelength of 0.3344 Å that was focused down to ~5 µm in diameter at the sample position. XRD patterns were recorded on a MarCCD detector where the DAC was rotated from –15° to + 15° about the X-ray beam direction with an interval of one degree. The tilting and rotation of the MarCCD detector relative to the incident X-ray beam were calibrated using lanthanum hexaboride (LaB_6) powder as the X-ray diffraction standard. The calibrated distance between sample and MarCCD detector was 196.79 mm. XRD images were processed and integrated using the Fit2D software for deriving the lattice parameters of the pressure calibrant polycrystalline Pt (Hammersley et al. 1996). The same piece of sample was used for ambient and high-pressure experiments. The different phases and lattice parameters of $MnCO_3$ were extracted by the GSE_ADA/RSV software packages (Supplementary Table[1] S1) (Dera et al. 2013). Pressure was calculated from the Pt pressure calibrant using a third-order Birch-Murnaghan equation of state (BM EoS) (Fei et al. 2007).

Laser Raman spectroscopy

High-pressure laser Raman spectra of $CaCO_3$ and $MnCO_3$ were collected using a Renishaw RM1000 Raman microscope equipped with a 250 mm spectrometer focal length in the Extreme Environments Laboratory (EEL) at Stanford University. The Raman system uses a 514.5 nm laser excitation line and has a spectral resolution of 4 cm^{-1} with the holographic diffraction grating of 1800 lines/mm. The laser with a maximum power of 25 mW was focused through a Nikon L Plan EPI 20X, 0.35 objective onto the sample with the laser spot of approximately 2 µm in diameter. The Raman spectra were collected between –450 to +1600 cm^{-1}. The single-crystal samples of ~10 µm thick and ~40 µm in diameter were loaded into the sample chamber of a DAC with the (101) crystal plane facing the incident laser beam, together with a few ruby spheres as the pressure calibrant (Mao et al. 1986). Helium was loaded into the sample chamber as the pressure-transmitting medium using the high-pressure gas loading system in the EEL. Pressure and uncertainties were determined by averaging over multiple measurements of ruby spheres before and after each Raman spectrum. We note that the Raman spectra of the sample for XRD experiments were measured during decompression, indicating that the high-pressure phase transition of $MnCO_3$ was reversible. Raman spectra were processed using the software PeakFit v4.12 with the Voigt area method.

Theoretical methods

Theoretical Raman spectra were computed at 0 K using the density-functional perturbation theory (Baroni and Resta 1986; Baroni et al. 2001; Gonze et al. 2005) in the ABINIT implementation (Veithen et al. 2005; Gonze et al. 2009) with planewaves and pseudopotentials. We used experimental input for the starting configurations of the crystal structures for $CaCO_3$-I (Graf 1961), $CaCO_3$-III (Pippinger et al. 2015), and $CaCO_3$-VI (Merlini et al. 2012b). We used Troullier-Martins-type pseudopotentials to describe the core electrons (Fuchs and Scheffler 1999). We employed 12 electronic bands per $CaCO_3$ formula unit. The first Brillouin zone of the reciprocal space was sampled using 8 × 8 × 8, 4 × 4 × 4, and 6 × 6 × 6 regular grids of **k**-points (Monkhorst and Pack 1976) for, respectively the three structures. Together with a kinetic energy cutoff of 40 Ha (1 Ha = 27.2116 eV) this converged the energy at better than 1 mHa per unit cell. The structures were first relaxed at the target pressure, i.e., the atoms are displaced and the unit-cell shape and volume are allowed to change under symmetry constraints until the forces are minimized and the stresses have only hydrostatic components. The Raman spectra were calculated on the relaxed structures: the position of the peaks comes from the quasi-harmonic approximation, and the reported intensity of the peaks is the average of the Raman tensors over all possible crystal orientations and laser polarizations, as for ideal powders. More details can be found in the WURM project original reference (Caracas and Bobocioiu 2011) and web site (http://wurm.info), including the spectra and the corresponding atomic displacement patterns.

Results and Discussion

We conducted two experimental runs and obtained the single-crystal XRD patterns for $MnCO_3$ up to 67 GPa at 300 K. The XRD patterns demonstrated that the rhombohedral $MnCO_3$-I was stable up to 45 GPa at ambient temperature (Figs. 1–2). At higher pressures, the XRD patterns of $MnCO_3$ changed (Fig. 1 insets). The X-ray diffraction spots of $MnCO_3$ at 48–67 GPa could be well indexed to the crystal structure of $CaCO_3$-VI (Merlini et al. 2012a). Laser Raman spectra of $CaCO_3$ and $MnCO_3$ were collected with pressure steps of 1–3 GPa up to 53 and 75 GPa, respectively (Figs. 3–4). Raman spectra for $CaCO_3$ changed around 2 and 15 GPa, respectively, while those for $MnCO_3$ started changes around 44 and 46 GPa. For $CaCO_3$, Raman spectra were assigned to $CaCO_3$-I below 1.9 GPa, to $CaCO_3$-III between 1.9–15 GPa, and to $CaCO_3$-VI above 15 GPa, respectively. For $MnCO_3$, Raman spectra were assigned to $MnCO_3$-I below 44 GPa and to $MnCO_3$-II above 47 GPa, and to a mixture of these two in between. Vibrational modes of $CaCO_3$ in the $CaCO_3$-I, $CaCO_3$-III, and $CaCO_3$-VI structure were theoretically calculated to better understand the observed Raman bands at high pressures (Figs. 5–6; see Tables S2–S4 in Supplementary Materials[1] for more details).

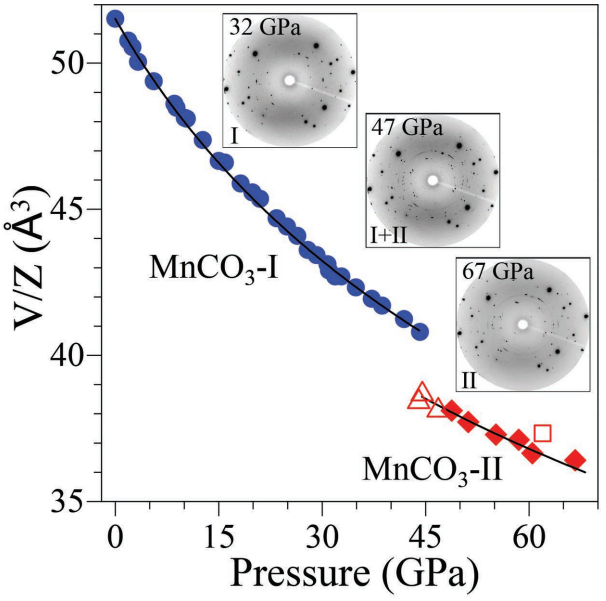

Figure 1. The pressure-volume relations of $MnCO_3$-I and $MnCO_3$-II. Insert: X-ray diffraction images collected during a rotation of 30° at 32, 47, and 67 GPa, respectively, showing the sharp diffraction peaks of $MnCO_3$ at high pressures. The diffraction rings in the XRD patterns come from the pressure medium Ne while the $MnCO_3$ remained a single crystal across the phase transition. The diffraction images were illustrated by the DIOPTAS program (Prescher and Prakapenka 2015). Circles and diamonds: the unit-cell volume per formula (V/Z) for $MnCO_3$-I and $MnCO_3$-II from this study; square and triangles: V/Z of $MnCO_3$-II by Boulard et al. (2015) and Merlini et al. (2015), respectively; lines: BM EoS fits to the data. Error bars smaller than symbols are not shown for clarity. See Table S1 in Supplementary Materials[1] for more details. (Color online.)

[1]Deposit item AM-16-125742, Supplementary Tables. Deposit items are free to all readers and found on the MSA web site, via the specific issue's Table of Contents (go to http://www.minsocam.org/msa/ammin/toc/2016/Dec2016_data/Dec2016_data.html).

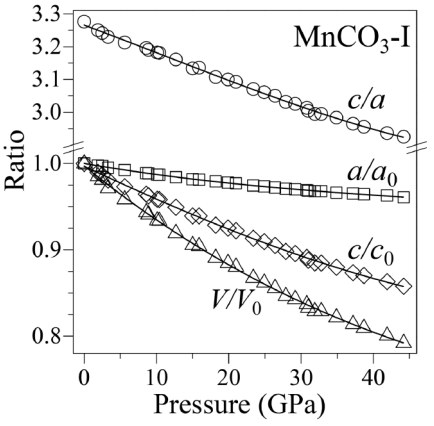

FIGURE 2. The relative axial compressibilities of the rhombohedral phase of $MnCO_3$-I as a function of pressure. Circles, squares, diamonds, and triangles: c/a, a/a_0, c/c_0, and V/V_0, respectively. Error bars smaller than symbols are not shown for clarity.

Equation of state and compressibility of $MnCO_3$

The pressure-volume (P-V) curve between 0 and 44 GPa was fit to a third-order BM EoS to derive the elastic parameters of $MnCO_3$-I, yielding the zero bulk modulus K_0 = 122(3) GPa and the pressure derivative of bulk modulus K' = 3.7(2), or K_0 = 113(3) GPa if K' was fixed at 4, with the zero unit-cell volume V_0 = 309.1(1) Å^3 from XRD measurements at ambient conditions (Supplementary Table[1] S1). The derived EoS parameters in this study are comparable to most previous studies (Zhang and Reeder 1999; Boulard et al. 2015; Merlini et al. 2015), but slightly lower than those of $MnCO_3$ reported by Ono (2007). The discrepancy may be due to the lack of a pressure medium and fewer data points in the study by Ono (2007).

The relative axial compressibilities, a/a_0 and c/c_0, and the axial ratio, c/a, of $MnCO_3$-I were determined as a function of pressure up to 44 GPa (Fig. 2). The compressibility of $MnCO_3$-I is not isotropic, with the a axis about 3–4 times less compressible than the c axis, which is consistent with the results reported by Boulard et al. (2015). The anisotropic change in the a and c axes causes the octahedral distortion to change from trigonally elongated to trigonally compressed with increasing pressure (Lavina et al. 2010). The $(Mg,Fe)CO_3$ solid-solution series exhibits a similar anisotropic behavior in the a/a_0 and c/c_0 ratios at high pressures (Lavina et al. 2010). The a/a_0 and c/c_0 values were approximately 0.96 and 0.86, respectively, for $MgCO_3$, $FeCO_3$, and $MnCO_3$ at ~40 GPa (e.g., Zhang et al. 1998; Fiquet et al. 2002; Litasov et al. 2008; Lavina et al. 2010; Lin et al. 2012). The comparable axis compressibilities of $MgCO_3$, $FeCO_3$, and $MnCO_3$ are likely due to them having the same structure.

$MnCO_3$-I started to transform into $MnCO_3$-II at 45 GPa and the phase transition was completed at 48 GPa. A complex diffraction pattern was observed at 47 GPa (Fig. 1 insert), which cannot be indexed solely by $MnCO_3$-I or $MnCO_3$-II. This pattern contained both phases, indicating that $MnCO_3$-I and $MnCO_3$-II could coexist prior to the completion of phase transition. The observed transition pressure of $MnCO_3$ in this study is a few GPa higher than that of $(Mn_{0.96}Ca_{0.04})CO_3$ reported by Merlini et al.

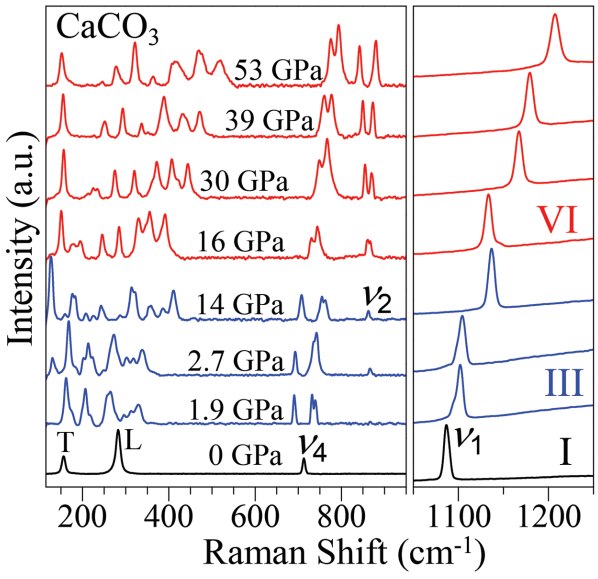

FIGURE 3. Representative Raman spectra of $CaCO_3$ at high pressures and 300 K. The metastable $CaCO_3$-II phase was not observed likely due to the small pressure range over which this phase is stable and the relatively large pressure steps. Raman modes of $CaCO_3$-I are labeled according to White (1974). T = translational lattice mode; L = librational lattice mode; $\nu_4 = CO_3$ in-plane bend; $\nu_2 = CO_3$ out-of-plane bend; $\nu_1 = CO_3$ symmetric stretch. (Color online.)

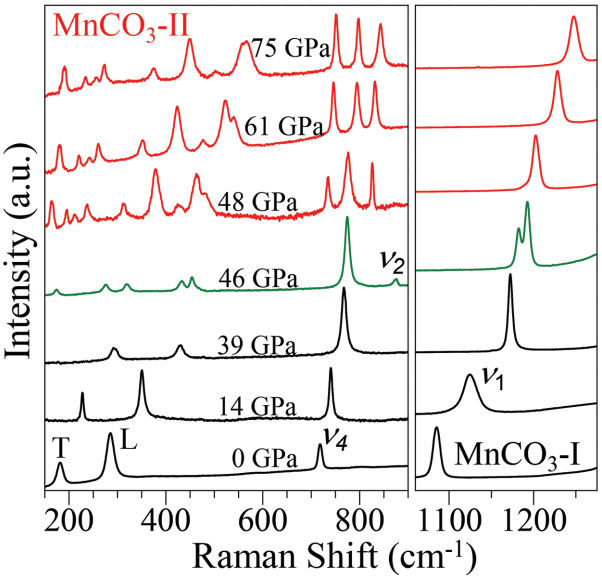

FIGURE 4. Representative Raman spectra of $MnCO_3$ at high pressures. $MnCO_3$ transformed from the low-pressure phase ($MnCO_3$-I) to the high-pressure phase ($MnCO_3$-II) at 44–47 GPa. Raman modes of $MnCO_3$-I are labeled accordingly as T, L, ν_4, and ν_1. The splitting of Raman bands of $MnCO_3$ at 46 GPa corresponds to the coexisting phases of I and II revealed by XRD measurements at 47 GPa (Fig. 1 insert) with the ν_2 peak possibly at ~875 cm^{-1}. (Color online.)

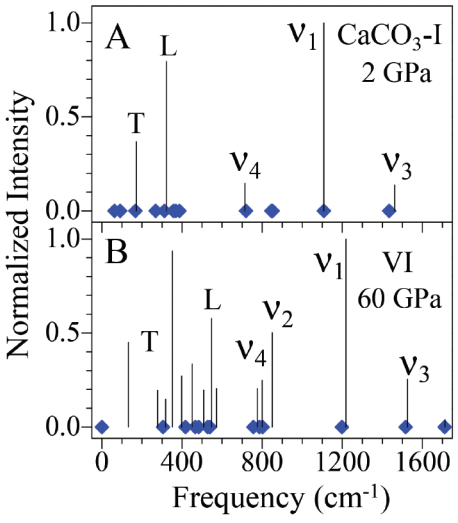

FIGURE 5. Vibrational modes of $CaCO_3$-I and VI as a function of frequency at high pressures by theoretical calculations. The intensity was normalized using the intensity of ν_1 as the reference. The blue diamonds indicate that the calculated intensity of modes are extremely weak (see Supplementary[1] Tables S2 and S4 for more details). (Color online.)

(2015), indicating that a small amount of Ca^{2+} might effectively reduce the transition pressure in the $(Ca,Mn)CO_3$ solid-solution system. We note that Farfan et al. (2013) and Boulard et al. (2015) reported a transition of $MnCO_3$ between 15 and 35 GPa using NaCl or silicon oil as the pressure-transmitting medium and that this transition is not consistent with the $CaCO_3$-II and $CaCO_3$-VI structures and may be related to a distortion of the $CaCO_3$-I structure due to nonhydrostatic conditions, especially when NaCl undergoes a B1 to B2 phase transition about 25–30 GPa, which involves a fairly large volume change. In contrast, both Merlini et al. (2015) and this study used Ne and/or He as a pressure-transmitting medium in the single-crystal XRD measurements and did not observe the distorted phase of the $CaCO_3$-I structure between 15 and 30 GPa. Similarly, Ono (2007) did not observe this distorted phase likely because the $MnCO_3$ sample was annealed to 1000–1500 K to relax any differential stress at high pressures. In particular, Merlini et al. (2015) observed $MnCO_3$ in the $CaCO_3$-VI structure at ~36 GPa during decompression, while Boulard et al. (2015) observed the presence of diffraction peaks other than from $MnCO_3$-I above ~35 GPa in the power XRD patterns using NaCl as the pressure-transmitting medium. To date, the transition pressure of $MnCO_3$ into the $CaCO_3$-VI structure has been reported ranging approximately from 35–50 GPa, which seems sensitive to the stress field in the sample chambers. In addition, Santillan and Williams (2004) did not observe any phase transition up to 50 GPa, likely because the incorporation of 16 mol% of Fe^{2+} and Mg^{2+} in their $MnCO_3$ sample could greatly enlarge the stability field of the calcite structure of $MnCO_3$. The addition of Fe and Mg into $MnCO_3$ could thus greatly enlarge the stability field of calcite structured $MnCO_3$. This is similar to the idea presented by Shi et al. (2012) that an increase in Mn concentration in $CaCO_3$ expanded the high-pressure stability range of the different $CaCO_3$ structures.

The *P-V* curve of $MnCO_3$-II was fit to a second-order BM EoS from 48 to 67 GPa, resulting in $K_0 = 144(13)$ GPa and $V_0 = 285(7)$ Å^3 with K' fixed at 4. The unit-cell volume per formula (*V/Z*) of $MnCO_3$-II reported by Merlini et al. (2015) is close to the *P-V* curve extrapolated by the current EoS of $MnCO_3$-II. The bulk modulus of $MnCO_3$ increases by approximately 12% across the phase transition from I to II. The density of $MnCO_3$ showed a dramatic increase by ~5.5% from $MnCO_3$-I to $MnCO_3$-II, in good agreement with Merlini et al. (2015), while the density increased only by ~2% at 35 GPa reported by Boulard et al. (2015). We note that the *V/Z* at 62 GPa measured by Boulard et al. (2015) (corresponding to the red square in Fig. 1) is approximately 2% larger than that from the current EoS of $MnCO_3$-II. Such a large discrepancy may suggest that the unit cell of $MnCO_3$-II in the triclinic system may be overestimated due to the overlap and insufficient diffraction lines in the powder XRD patterns by Boulard et al. (2015).

Vibrational properties of $CaCO_3$ and $MnCO_3$

Four Raman modes were observed in the $CaCO_3$-I phase of $CaCO_3$ and $MnCO_3$, including the translational lattice mode

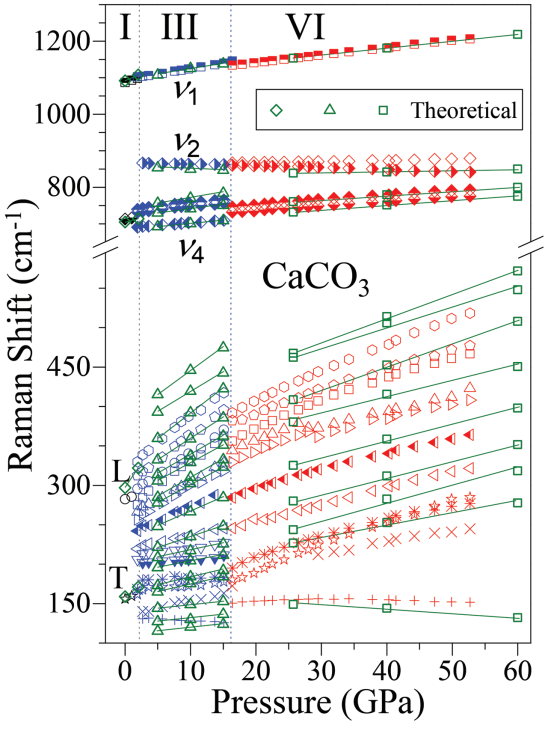

FIGURE 6. Raman shifts of $CaCO_3$ at high pressures. Black, blue, and red symbols = experimental observations of $CaCO_3$-I, $CaCO_3$-III, and $CaCO_3$-VI, respectively; olive diamonds, triangles, and squares = theoretical calculations of $CaCO_3$-I, $CaCO_3$-III, and $CaCO_3$-VI, respectively (this study). The calculated modes with the extremely weak intensities (blue diamonds in Fig. 5) are not shown for clarity. The calculated 75 Raman peaks of $CaCO_3$-III were selectively plotted for comparison. The two vertical dotted lines indicate the approximate phase transition pressures. The solid lines represent the linear fits to the calculations. Error bars are typically smaller than symbols. See Supplementary Tables S2–S5[1] for more details. (Color online.)

TABLE 1. Experimental vibrational parameters of $CaCO_3$ at high pressures

$CaCO_3$	Raman mode	Initial frequency[a] (cm^{-1})	dν/dP (cm^{-1}/GPa)	Mode Grüneisen parameter (γ_i)
I	T	156	2.52(8)	1.14(4)
I	L	282	5.19(17)	1.33(6)
I	ν_4	713	2.35(7)	0.23(1)
I	ν_1	1086	5.96(15)	0.39(2)
III	T	131	–0.35(6)	–0.34(7)
III	T	140	1.98(10)	1.66(9)
III	T	161	0.76(11)	0.56(9)
III	T	168	0.36(6)	0.25(5)
III	T	202	0.56(4)	0.35(4)
III	T	206	0.89(13)	0.52(9)
III	T	219	1.91(21)	1.04(13)
III	L	242	3.78(18)	1.78(11)
III	L	256	4.41(29)	1.90(15)
III	L	266	4.32(17)	1.82(9)
III	L	275	6.31(26)	2.46(12)
III	L	296	5.76(25)	2.17(11)
III	L	312	6.25(33)	2.21(17)
III	L	330	6.28(32)	2.08(15)
III	ν_4	689	1.35(8)	0.23(2)
III	ν_4	731	1.31(17)	0.22(3)
III	ν_4	739	1.33(17)	0.22(3)
III	ν_2	866	–0.29(3)	–0.04(1)
III	ν_1	1102	2.78(14)	0.31(3)
VI	T	150	0.01(1)	0.01(1)
VI	T	172	1.37(22)	1.56(30)
VI	T	180	2.87(45)	3.03(57)
VI	T	195	2.17(49)	2.22(55)
VI	T	245	2.06(21)	1.81(20)
VI	L	284	2.04(26)	1.54(21)
VI	L	329	2.21(57)	1.48(46)
VI	L	343	1.98(62)	1.29(45)
VI	L	356	3.08(33)	1.83(24)
VI	L	382	2.82(29)	1.62(20)
VI	L	391	3.45(21)	1.87(15)
VI	ν_4	732	1.19(9)	0.39(5)
VI	ν_4	746	1.19(9)	0.39(5)
VI	ν_2	860	–0.48(7)	–0.14(3)
VI	ν_2	867	0.33(7)	0.09(2)
VI	ν_1	1134	2.04(12)	0.44(3)

[a] Initial frequencies of Raman modes for $CaCO_3$-I, $CaCO_3$-III, and $CaCO_3$-VI are at 0, 1.9, and 16 GPa, respectively.

TABLE 2. Experimental vibrational parameters of $MnCO_3$ at high pressures

$MnCO_3$	Raman mode	Initial frequency[a] (cm^{-1})	dν/dP (cm^{-1}/GPa)	Mode Grüneisen parameter (γ_i)
I	T	184	2.91(5)	2.37(7)
I	L	290	3.68(9)	1.99(8)
I	ν_4	719	1.28(6)	0.33(3)
I	ν_1	1086	2.17(7)	0.38(3)
II	T	165	0.89(6)	1.93(17)
II	T	203	1.09(8)	1.91(19)
II	T	220	1.33(10)	2.15(18)
II	T	244	1.01(8)	1.50(14)
II	T	324	1.83(5)	2.02(8)
II	L	391	2.05(11)	1.87(11)
II	L	442	2.12(21)	1.72(19)
II	L	481	2.70(16)	2.01(19)
II	L	503	2.48(19)	1.78(22)
II	ν_4	735	0.51(4)	0.26(4)
II	ν_4	782	0.58(10)	0.28(6)
II	ν_4	826	0.63(8)	0.29(5)
II	ν_1	1202	1.72(8)	0.54(9)

[a] Initial frequencies of Raman modes for $MnCO_3$-I and $MnCO_3$-II are at 0 and 48 GPa, respectively.

E_g (T), librational lattice mode E_g (L), CO_3 in-plane bend mode E_g (ν_4), and CO_3 symmetric stretch mode A_{1g} (ν_1) consistent with previous studies (e.g., White 1974; Shi et al. 2012; Farfan et al. 2013). The frequencies of the Raman modes of $CaCO_3$-I at ambient conditions and their pressure dependence (dν/dP) are consistent with literature results (Table 1) (Liu and Mernagh 1990; Gillet et al. 1993). Calculations show the existence of five Raman peaks with intermediate to strong intensities (Fig. 5 and Supplementary[1] Table S2). The highest frequency stretching mode E_g (ν_3) overlaps with the diamond Raman peak. The frequencies of the Raman modes of $MnCO_3$-I at ambient conditions are consistent with previous work by Shi et al. (2012). The dν/dP of $MnCO_3$-I is comparable to Farfan et al. (2013), although their frequencies are systematically higher by ~10 cm^{-1} possibly caused by the systematic error due to the incorrect setting of the zero position (Table 2).

The combined XRD and Raman results on $CaCO_3$ and $MnCO_3$ from this study and Merlini et al. (2012b) were used to derive the mode Grüneisen parameters (γ_i). The vibrational frequency (ν) as a function of V or P represents the mode Grüneisen parameter for a phonon mode following the relation (Born and Huang 1954):

$$\gamma_i = -\frac{d\ln\nu}{d\ln V} = \frac{K_T}{\nu}\left(\frac{d\nu}{dP}\right),$$

where K_T is the isothermal bulk modulus. The mode Grüneisen parameters describe the effect that changing the volume of a crystal lattice volume has on its vibrational properties. The γ_i for two external modes (T and L) of $MnCO_3$-I are approximately 2.37 and 1.99, respectively, approximately twice that of $CaCO_3$-I (Tables 1–2). The γ_i for the internal mode ν_1 of $CaCO_3$-I is about 0.39, comparable to that for $MnCO_3$-I, $FeCO_3$-I, and $MgCO_3$-I (Liu and Mernagh 1990; Gillet et al. 1993; Lin et al. 2012). The γ_i for the internal mode ν_4 of $CaCO_3$-I is approximately 30% less than that of $MnCO_3$-I. The γ_i for ν_4 of $MnCO_3$-I of approximately 0.33 agrees well with infrared measurements by Boulard et al. (2015), while Santillan and Williams (2004) reported a much smaller γ_i value for the ν_4 of $MnCO_3$-I likely due to a large amount of Ca, Fe, and Mg (23 mol% in total) in their rhodochrosite sample. We note that Santillan and Williams (2004) suggested that ion substitution has a negligible effect on infrared frequencies (Dubrawski et al. 1989). However, this may be true for the room-pressure frequencies and not necessarily true for the pressure dependence of infrared modes.

The calculations showed the existence of 75 Raman-active modes in $CaCO_3$-III (Supplementary Table[1] S3). Most of these modes may overlap in the experimental spectrum. Experimentally we observed 19 and 16 Raman bands in $CaCO_3$-III and $CaCO_3$-VI, respectively. These Raman bands can be assigned to five different Raman modes, including T, L, ν_4, ν_1, and ν_2 (the CO_3 out-of-plane bend). The reduction in frequencies and the modification in the intensity of most of the Raman bands were observed when $CaCO_3$-III transformed into $CaCO_3$-VI at 14–16 GPa, likely a result of the differing orientation of the CO_3^{2-} group in the phases (Fig. 3). $CaCO_3$-III contains non-coplanar CO_3^{2-} groups with a layered structure, while $CaCO_3$-VI is characterized by coplanar CO_3^{2-} groups with a non-layered structure (Merlini et al. 2012b). Williams et al. (1992) may have missed the phase transition from $CaCO_3$-III to $CaCO_3$-VI due to the large pressure steps in their high-pressure infrared measure-

ments. Fiquet et al. (1994) noted that there were changes in the powder diffraction patterns of $CaCO_3$-III starting near ~8 GPa, which might be explained by a new calcite structure, but they could not resolve the new structure and speculated that it could also be related to normal high-pressure features of $CaCO_3$-III. Catalli and Williams (2005) first recognized this phase transition at ~15 GPa and resolved the detailed changes in the carbonate v_4 mode using infrared spectroscopy and finer pressure steps. The lowest-frequency band of $CaCO_3$-III experimentally decreased in frequency with increasing pressure (Fig. 6; Table 1). Raman bands in the same vibrational mode of $CaCO_3$-III seem to have similar values of dv/dP, with <2 for T, approximately 4–6 for L, and about 1.3 for v_4. The new band of 866 cm^{-1} at 1.9 GPa was assigned to the v_2 of $CaCO_3$-III, having a negative γ_i and dv/dP of approximately –0.3, which is also observed in calculations (Fig. 6). It is in line with infrared measurements by Williams et al. (1992), which is close to a zero pressure shift of the v_2 of $CaCO_3$-III reported by Catalli and Williams (2005). The negative dv/dP of v_2 could be explained by the increase in the coupling of neighboring CO_3^{2-} groups, while the positive dv/dP of v_4 could be due to an increase in the Mn-O bond strength (Kraft et al. 1991). The dv/dP for the v_1 band decreases by approximately 50% from $CaCO_3$-I to $CaCO_3$-III.

Theoretical calculations predict there are 30 active vibrational bands in $CaCO_3$-VI (Fig. 5). Fourteen of them may not be experimentally observed due to their weak intensities at high pressures (see Supplementary Table[1] S4 for more details). The high-frequency vibrational modes at 1400–1650 cm^{-1} were not experimentally observed in this study because of their superposition with the diamond Raman peak. The v_1 of $CaCO_3$-VI from theoretical calculations agree perfectly with experiment observations (Fig. 6). Both suggested that the dv/dP for the v_1 band decreases approximately by 30% from $CaCO_3$-III to $CaCO_3$-VI. Furthermore, one v_2 band of $CaCO_3$-III diverged into two v_2 bands of $CaCO_3$-VI, while theoretical calculations only predict one v_2 band with a small positive dv/dP value close to zero. For $CaCO_3$-VI, the lower-frequency v_2 band at 860 cm^{-1} experimentally had a negative dv/dP of approximately –0.5, but the higher-frequency v_2 band at 867 cm^{-1} had a positive dv/dP of approximately +0.3. We note that Catalli and Williams (2005) observed one v_2 peak of $CaCO_3$-VI having an unchanged position near 870 cm^{-1} throughout infrared measurements up to 52 GPa. The dv/dP values of $CaCO_3$-VI for the T bands from experimental measurements are around 2, for the L bands at 2–3.5, and for the v_4 bands approximately at 1.2, which are comparable to those from theoretical calculations.

Although they are isostructural, the number and relative intensity of the Raman bands observed in $MnCO_3$-II are not the same as $CaCO_3$-VI (Figs. 3–4). The difference in the Raman spectra of the $CaCO_3$-VI-structured $CaCO_3$ and $MnCO_3$ suggests that cations (e.g., Mn^{2+} and Ca^{2+}) can have more dramatic effects on the vibrational modes in the high-pressure $CaCO_3$-VI phase than the rhombohedral $CaCO_3$-I phase. All 13 Raman bands of $MnCO_3$-II monotonically increased in frequency with increasing pressure (Fig. 7; Table 2). The dv/dP of $MnCO_3$-II for the T bands are at 1–2 and for the L bands at 2–2.5. All the T and L Raman bands have the value of γ_i at ~2. Three Raman bands for $MnCO_3$-II in 700–850 cm^{-1} display a comparable dv/dP of ~0.55 and γ_i of ~0.28, and were thus assigned to v_4. The v_2 band at 873 cm^{-1} only appears between 44–47 GPa, and likely becomes too weak after the completion of the phase transformation to $MnCO_3$-II to be observed. The Raman spectra collected at 44–47 GPa exhibit the peak splitting of Raman bands within the pressure range where we observed coexistence of $MnCO_3$-I and $MnCO_3$-II according to X-ray diffraction patterns (Fig. 1 insert and Fig. 4). Two v_1 Raman bands were observed at 46 GPa, likely with one coming from $MnCO_3$-I and the other from $MnCO_3$-II. Farfan et al. (2013) observed such splitting of v_1 from 48.2 to 55.2 GPa, indicating that $MnCO_3$-I and $MnCO_3$-II coexisted at a larger pressure range

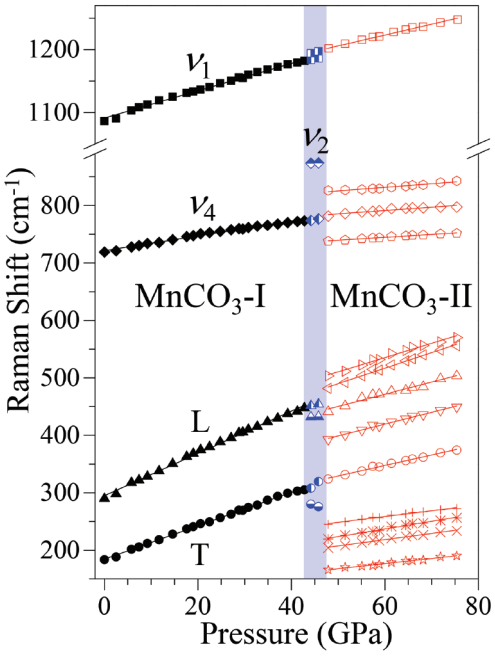

FIGURE 7. Raman shifts of $MnCO_3$ at high pressures. Solid, half-filled, and open symbols: $MnCO_3$-I, the coexisting phases of I and II, and $MnCO_3$-II, respectively; blue shaded area: the coexisting phases of I and II; solid lines: linear fits to experimental data. Error bars are typically smaller than symbols and are not shown for clarity. See Supplementary[1] Table S6 for more details. (Color online.)

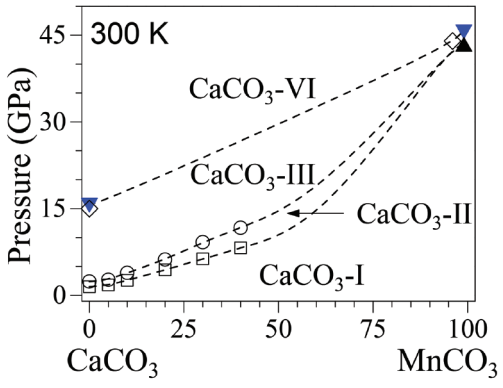

FIGURE 8. Schematic phase relations of the $(Mn,Ca)CO_3$ solid-solution series at 300 K. Dashed lines represent the tentative phase boundaries. Solid triangles = this study; diamonds = Merlini et al. (2012, 2015); squares and circles = Shi et al. (2012). (Color online.)

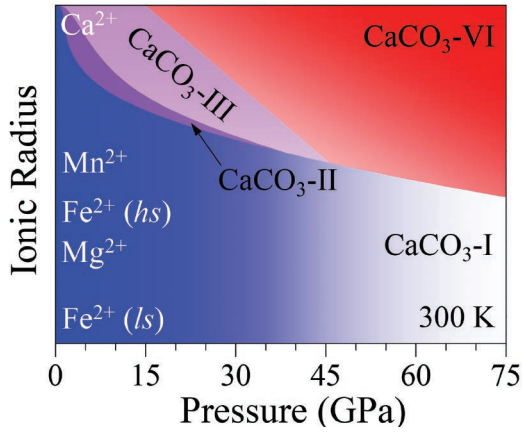

FIGURE 9. Schematic phase relations of the (Ca,Mn,Fe,Mg)CO_3 solid-solution system under high pressures at 300 K. The effective ionic radii of Ca^{2+}, Mn^{2+}, Fe^{2+}, and Mg^{2+} at ambient conditions are illustrated accordingly from Shannon (1976). *hs* = the high-spin state of Fe^{2+}; *ls* = the low-spin state of Fe^{2+}. (Color online.)

due to the use of silicon oil as the pressure-transmitting medium. The dv/dP of v_1 for $MnCO_3$-II is about 1.72, in good agreement with the infrared measurements by Boulard et al. (2015). We note that Raman peak splitting in $MnCO_3$-I at 44–47 GPa might suggest a subtle distortion of the $CaCO_3$-I structure between $MnCO_3$-I and $MnCO_3$-II, which may be similar to the change from the $CaCO_3$-III and $CaCO_3$-IIIb structures (Merlini et al. 2012b), although this potential transition cannot be resolved from the diffraction patterns in this study.

IMPLICATIONS

The phase stability of divalent metal carbonates (MCO_3) is significantly affected by compositional variation in the metal cations (M^{2+}). Previous studies suggested the $CaCO_3$-I phase stability of the (Mn,Ca)CO_3 solid solution was greatly enhanced by adding Mn^{2+} (Shi et al. 2012). For the Mn-rich (Mn,Ca)CO_3 compositions, the solid solution may directly transform into the $CaCO_3$-VI structure without going through $CaCO_3$-II and $CaCO_3$-III at high pressures (Fig. 8) (Boulard et al. 2015; Merlini et al. 2015). The phase transition pressure for $MnCO_3$ increased by approximately 2–3 GPa with an additional 2 mol% Mn^{2+} and 1 mol% Fe^{2+} replacing Ca^{2+} in $(Mn_{0.96}Ca_{0.04})CO_3$ (Merlini et al. 2015). The presence of 7 mol% Mg^{2+} and 9 mol% Fe^{2+} in (Mn,Ca)CO_3 could stabilize the $CaCO_3$-I phase at ~50 GPa and 2000 K (Santillan and Williams 2004). Furthermore, $MgCO_3$ can stabilize the $CaCO_3$-I structure up to at least 110 GPa at 2000 K (Isshiki et al. 2004), while $FeCO_3$ undergoes an isostructural spin transition around 45 GPa and remains in the $CaCO_3$-I structure to above 100 GPa at ambient temperature (e.g., Lavina et al. 2010; Farfan et al. 2012; Liu et al. 2014, 2015). In (Mn,Ca)CO_3, the radii of Ca^{2+} (100 pm) and Mn^{2+} (83 pm) are greater than that of Mg^{2+} (72 pm) and Fe^{2+} (78 and 61 pm for the high-spin and low-spin states, respectively) (Shannon 1976). The incorporation of a smaller cation into $CaCO_3$ increases the stability field of $CaCO_3$-I (Fig. 9).

The phase stability and high-pressure polymorph(s) of MCO_3 under Earth's mantle conditions have been an area of active debate. The lower-mantle oxygen fugacity may be at the Ni/NiO or Fe/FeO buffer making carbonates unstable in the deep mantle (see review by Frost and McCammon 2008). However, considering the uncertainty in our knowledge of lower-mantle oxygen fugacity, carbonates may be transported into the lower mantle by subducting slabs if the local oxygen fugacity is favorable for their survival. One piece of evidence is the observation of carbonate-bearing inclusions in diamonds that were potentially brought up to the Earth's surface from the deep mantle (Berg 1986; Wang et al. 1996; Walter et al. 2011). The high-pressure polymorph $CaCO_3$-VI has a smaller V/Z than aragonite up to at least 40 GPa and may replace aragonite in the Earth's mantle (Merlini et al. 2012b). The $CaCO_3$-VI-structured (Ca,Mn)CO_3 is stable up to at least 75 GPa at room temperature according to Raman spectra in this study. The incorporation of smaller cations (e.g., Mg^{2+}, Fe^{2+}, and Mn^{2+}) can significantly reduce the V/Z of $CaCO_3$-I and $CaCO_3$-VI, and thus may enhance the stability field of $CaCO_3$-rich carbonate in the $CaCO_3$-I and $CaCO_3$-VI structures inside cold, subducting slabs in the deep mantle that carried various limestone and carbonaceous sediments.

ACKNOWLEDGMENTS

We acknowledge R. McCarty, X. Wu, P. Dera, and R. Jones for experimental assistance and helpful discussion. W.L. Mao acknowledges support from the Geophysics Program at NSF (EAR 1446969) and the Deep Carbon Observatory. R. Caracas acknowledges computational support from eDARI under grant stl2816 and from PSMN of ENS Lyon, and financial support from the PICS program of CNRS and the Deep Carbon Observatory. D.W. Fan acknowledges financial support from the National Natural Science Foundation of China (41374107), and the Youth Innovative Technology Talents Program of Institute of Geochemistry, Chinese Academy of Sciences. Portions of this work were performed at GeoSoilEnviroCARS (Sector 13) and HPCAT (Sector 16), Advanced Photon Source (APS), Argonne National Laboratory. Use of the COMPRES-GSECARS gas loading system was supported by COMPRES under NSF Cooperative Agreement EAR 11-57758 and by GSECARS through NSF grant EAR-1128799 and DOE grant DE-FG02-94ER14466. HPCAT operations are supported by DOE-NNSA under Award No. DE-NA0001974 and DOE-BES under Award No. DE-FG02-99ER45775, with partial instrumentation funding by NSF. The Advanced Photon Source, a U.S. Department of Energy (DOE) Office of Science User Facility is operated for the DOE Office of Science by Argonne National Laboratory under Contract No. DE-AC02-06CH11357. Data used in this study are available upon request from J. Liu (E-mail: jinliu1@stanford.edu) and R. Caracas (E-mail: razvan.caracas@ens-lyon.fr).

REFERENCES CITED

Baroni, S., and Resta, R. (1986) Ab initio calculation of the low-frequency Raman cross section in silicon. Physical Review B, 33, 5969–5971.
Baroni, S., de Gironcoli, S., Dal Corso, A., and Giannozzi, P. (2001) Phonons and related crystal properties from density-functional perturbation theory. Review of Modern Physics, 73, 515–562.
Berg, G.W. (1986) Evidence for carbonate in the mantle. Nature, 324, 50–51.
Biellmann, C., Gillet, P., Guyot, F.O., Peyronneau, J., and Reynard, B. (1993) Experimental evidence for carbonate stability in the Earth's lower mantle. Earth and Planetary Science Letters, 118, 31–41.
Born, M., and Huang, K. (1954) Dynamical theory of crystal lattices. Oxford University Press, U.K.
Boulard, E., Goncharov, A.F., Blanchard, M., and Mao, W.L. (2015) Pressure-induced phase transition in $MnCO_3$ and its implications on the deep carbon cycle. Journal of Geophysical Research: Solid Earth, 120, 4069–4079.
Caracas, R., and Bobocioiu, E. (2011) The WURM project—a freely available web-based repository of computed physical data for minerals. American Mineralogist, 96, 437–444.
Catalli, K., and Williams, Q. (2005) A high-pressure phase transition of calcite-III. American Mineralogist, 90, 1679–1682.
Dasgupta, R., and Hirschmann, M.M. (2010) The deep carbon cycle and melting in Earth's interior. Earth and Planetary Science Letters, 298, 1–13.
Dera, P., Zhuravlev, K., Prakapenka, V., Rivers, M.L., Finkelstein, G.J., Grubor-Urosevic, O., Tschauner, O., Clark, S.M., and Downs, R.T. (2013) High pressure single-crystal micro X-ray diffraction analysis with GSE_ADA/RSV software. High Pressure Research, 33, 466–484.
Dubrawski, J.V., Channon, A.-L., and Warne, S.S. (1989) Examination of the

siderite-magnesite mineral series by Fourier transform infrared spectroscopy. American Mineralogist, 74, 187–190.
Farfan, G., Wang, S., Ma, H., Caracas, R., and Mao, W.L. (2012) Bonding and structural changes in siderite at high pressure. American Mineralogist, 97, 1421–1426.
Farfan, G.A., Boulard, E., Wang, S., and Mao, W.L. (2013) Bonding and electronic changes in rhodochrosite at high pressure. American Mineralogist, 98, 1817–1823.
Fei, Y., Ricolleau, A., Frank, M., Mibe, K., Shen, G., and Prakapenka, V. (2007) Toward an internally consistent pressure scale. Proceedings of the National Academy of Sciences, 104, 9182–9186.
Fiquet, G., Guyot, F., and Itie, L.P. (1994) High-pressure X-ray diffraction study of carbonates: $MgCO_3$, $CaMg(CO_3)_2$, and $CaCO_3$. American Mineralogist, 79, 15–23.
Fiquet, G., Guyot, F., Kunz, M., Matas, J., Andrault, D., and Hanfland, M. (2002) Structural refinements of magnesite at very high pressure. American Mineralogist, 87, 1261–1265.
Frost, D.J., and McCammon, C.A. (2008) The redox state of Earth's mantle. Annual Review of Earth and Planetary Sciences, 36, 389–420.
Fuchs, M., and Scheffler, M. (1999) Ab initio pseudopotentials for electronic structure calculations of poly-atomic systems using density-functional theory. Computer Physics Communications, 119, 67–98.
Gillet, P., Biellmann, C., Reynard, B., and McMillan, P. (1993) Raman spectroscopic studies of carbonates part I: High-pressure and high-temperature behaviour of calcite, magnesite, dolomite and aragonite. Physics and Chemistry of Minerals, 20, 1–18.
Gonze, X., Rignanese, G.-M., and Caracas, R. (2005) First-principles studies of the lattice dynamics of crystals, and related properties. Zeitschrift für Kristallographie, 220, 458–472.
Gonze, X., Amadon, B., Anglade, P.M., Beuken, J.M., Bottin, F., Boulanger, P., Bruneval, F., Caliste, D., Caracas, R., Côté, M., and others. (2009) ABINIT: First-principles approach to material and nanosystem properties. Computer Physics Communications, 180, 2582–2615.
Graf, D.L. (1961) Crystallographic tables for the rhombohedral carbonates. American Mineralogist, 46, 1283–1316.
Hammersley, A.P., Svensson, S.O., Hanfland, M., Fitch, A.N., and Hausermann, D. (1996) Two-dimensional detector software: From real detector to idealised image or two-theta scan. High Pressure Research, 14, 235–248.
Hazen, R.M., and Schiffries, C.M. (2013) Why deep carbon? Reviews in Mineralogy and Geochemistry, 75, 1–6.
Ishizawa, N., Setoguchi, H., and Yanagisawa, K. (2013) Structural evolution of calcite at high temperatures: Phase V unveiled. Scientific Reports, 3, 2832.
Isshiki, M., Irifune, T., Hirose, K., Ono, S., Ohishi, Y., Watanuki, T., Nishibori, E., Takata, M., and Sakata, M. (2004) Stability of magnesite and its high-pressure form in the lowermost mantle. Nature, 427, 60–63.
Kraft, S., Knittle, E., and Williams, Q. (1991) Carbonate stability in the Earth's mantle: A vibrational spectroscopic study of aragonite and dolomite at high pressures and temperatures. Journal of Geophysical Research, 96, 17997–18009.
Lavina, B., Dera, P., Downs, R.T., Yang, W., Sinogeikin, S., Meng, Y., Shen, G., and Schiferl, D. (2010) Structure of siderite $FeCO_3$ to 56 GPa and hysteresis of its spin-pairing transition. Physical Review B, 82, 064110.
Lin, J.-F., Liu, J., Jacobs, C., and Prakapenka, V.B. (2012) Vibrational and elastic properties of ferromagnesite across the electronic spin-pairing transition of iron. American Mineralogist, 97, 583–591.
Litasov, K.D., Fei, Y., Ohtani, E., Kuribayashi, T., and Funakoshi, K. (2008) Thermal equation of state of magnesite to 32 GPa and 2073 K. Physics of the Earth and Planetary Interiors, 168, 191–203.
Liu, J., Lin, J.-F., Mao, Z., and Prakapenka, V.B. (2014) Thermal equation of state and spin transition of magnesiosiderite at high pressure and temperature. American Mineralogist, 99, 84–93.
——— (2015) High-pressure orthorhombic ferromagnesite as a potential deep-mantle carbon carrier. Scientific Reports, 5, 7640.
Liu, L.-G., and Mernagh, T.P. (1990) Phase transitions and Raman spectra of calcite at high pressures and room temperature. American Mineralogist, 75, 801–806.
Liu, L.-g., Lin, C.-C., and Yang, Y.-J. (2001) Formation of diamond by decarbonation of $MnCO_3$. Solid State Communications, 118, 195–198.
Mao, H.-K., Xu, J., and Bell, P.M. (1986) Calibration of the ruby pressure gauge to 800 kbar under quasi-hydrostatic conditions. Journal of Geophysical Research, 91, 4673–4676.
Merlini, M., Crichton, W.A., Hanfland, M., Gemmi, M., Müller, H., Kupenko, I., and Dubrovinsky, L. (2012a) Structures of dolomite at ultrahigh pressure and their influence on the deep carbon cycle. Proceedings of the National Academy of Sciences, 109, 13509–13514.
Merlini, M., Hanfland, M., and Crichton, W.A. (2012b) $CaCO_3$-III and $CaCO_3$-VI, high-pressure polymorphs of calcite: Possible host structures for carbon in the Earth's mantle. Earth and Planetary Science Letters, 333–334, 265–271.
Merlini, M., Hanfland, M., and Gemmi, M. (2015) The $MnCO_3$-II high-pressure polymorph of rhodocrosite. American Mineralogist, 100, 2625–2629.
Monkhorst, H.J., and Pack, J.D. (1976) Special points for Brillouin-zone integrations. Physical Review B, 13, 5188–5192.
Oganov, A.R., Glass, C.W., and Ono, S. (2006) High-pressure phases of $CaCO_3$: Crystal structure prediction and experiment. Earth and Planetary Science Letters, 241, 95–103.
Ono, S. (2007) High-pressure phase transformation in $MnCO_3$: a synchrotron XRD study. Mineralogical Magazine, 71, 105–111.
Ono, S., Kikegawa, T., Ohishi, Y., and Tsuchiya, J. (2005) Post-aragonite phase transformation in $CaCO_3$ at 40 GPa. American Mineralogist, 90, 667–671.
Ono, S., Kikegawa, T., and Ohishi, Y. (2007) High-pressure transition of $CaCO_3$. American Mineralogist, 92, 1246–1249.
Pippinger, T., Miletich, R., Merlini, M., Lotti, P., Schouwink, P., Yagi, T., Crichton, W.A., and Hanfland, M. (2015) Puzzling calcite-III dimorphism: Crystallography, high-pressure behavior, and pathway of single-crystal transitions. Physics and Chemistry of Minerals, 42, 29–43.
Prescher, C., and Prakapenka, V.B. (2015) DIOPTAS: a program for reduction of two-dimensional X-ray diffraction data and data exploration. High Pressure Research, 35(3), 223–230.
Santillan, J., and Williams, Q. (2004) A high-pressure infrared and X-ray study of $FeCO_3$ and $MnCO_3$: comparison with $CaMg(CO_3)_2$-dolomite. Physics of the Earth and Planetary Interiors, 143–144, 291–304.
Shannon, R.D. (1976) Revised effective ionic radii and systematic studies of interatomic distances in halides and chalcogenides. Acta Crystallographica, A32(5), 751–767.
Shi, W., Fleet, M.E., and Shieh, S.R. (2012) High-pressure phase transitions in Ca-Mn carbonates $(Ca,Mn)CO_3$ studied by Raman spectroscopy. American Mineralogist, 97, 999–1001.
Suito, K., Namba, J., Horikawa, T., Taniguchi, Y., Sakurai, N., Kobayashi, M., Onodera, A., Shimomura, O., and Kikegawa, T. (2001) Phase relations of $CaCO_3$ at high pressure and high temperature. American Mineralogist, 86, 997–1002.
Veithen, M., Gonze, X., and Ghosez, P. (2005) Nonlinear optical susceptibilities, Raman efficiencies, and electro-optic tensors from first-principles density functional perturbation theory. Physical Review B, 71, 125107.
Walter, M.J., Kohn, S.C., Araujo, D., Bulanova, G.P., Smith, C.B., Gaillou, E., Wang, J., Steele, A., and Shirey, S.B. (2011) Deep mantle cycling of oceanic crust: evidence from diamonds and their mineral inclusions. Science, 334, 54–57.
Wang, A., Pasteris, J.D., Meyer, H.O.A., and Dele-Duboi, M.L. (1996) Magnesite-bearing inclusion assemblage in natural diamond. Earth and Planetary Science Letters, 141(1–4), 293–306.
White, W.B. (1974) The carbonate minerals. In V.C. Farmer, Ed., Infrared Spectra of Minerals, p. 227–284. Mineralogical Society of Great Britain & Ireland, London.
Williams, Q., Collerson, B., and Knittle, E. (1992) Vibrational spectra of magnesite ($MgCO_3$) and calcite-III at high pressures. American Mineralogist, 77, 1158–1165.
Zhang, J., and Reeder, R.J. (1999) Comparative compressibilities of calcite-structure carbonates: Deviations from empirical relations. American Mineralogist, 84, 861–870.
Zhang, J., Martinez, I., Guyot, F., and Reeder, R.J. (1998) Effects of Mg-Fe^{2+} substitution in calcite-structure carbonates: Thermoelastic properties. American Mineralogist, 83, 280–287.

Manuscript received February 27, 2016
Manuscript accepted July 25, 2016
Manuscript handled by Martin Kunz